Supplementary Information

Determination of the In-Plane Exciton Radius in 2D CdSe Nanoplatelets *via* Magneto-Optical Spectroscopy

Alexandra Brumberg,[1] Samantha M. Harvey,[1,2] John P. Philbin,[3] Benjamin T. Diroll,[4] Byeongdu Lee,[5] Scott A. Crooker,[6] Michael R. Wasielewski,[1,2] Eran Rabani,[3,7,8] and Richard D. Schaller[1,4,*]

[1] Department of Chemistry, Northwestern University, Evanston, IL 60208, United States

[2] Institute for Sustainability and Energy at Northwestern, Northwestern University, Evanston, IL, 60208, United States

[3] Department of Chemistry, University of California, Berkeley, CA 94720, United States

[4] Center for Nanoscale Materials, Argonne National Laboratory, Lemont, IL 60439, United States

[5] Advanced Photon Source, Argonne National Laboratory, Lemont, IL 60439, United States

[6] National High Magnetic Field Laboratory, Los Alamos National Laboratory, Los Alamos, NM 87545, United States

[7] The Sackler Center for Computational Molecular and Materials Science, Tel Aviv University, Tel Aviv 69978, Israel

[8] Materials Science Division, Lawrence Berkeley National Laboratory, Berkeley, CA 94720, United States

* Corresponding author: schaller@anl.gov, schaller@northwestern.edu

Contents

Verification of the Low Magnetic Field Regime 3
Absorption Spectra of Samples 5
SAXS Data for 3 and 4 ML NPLs 6
Data Processing 8
Excitonic g-factors 10
Diamagnetic Shifts 12
Computational Details 13
Effect of Dielectric Constant on Exciton Lateral Extent 15
References 17

Verification of the Low Magnetic Field Regime

The formula presented for the diamagnetic shift in the main text of the paper (Eq. 2) is only valid for "low" magnetic fields, meaning the cyclotron energy of an exciton in a magnetic field is less than the binding energy of the exciton. (Alternatively, the strength of the magnetic field can be evaluated by comparing the magnetic length to the Bohr radius of the exciton.) This calculation must be executed for each NPL thickness, as the binding energy increases as the NPL thickness decreases.

Binding energies for 3, 4, and 5 ML CdSe NPLs are reported in Table S1 from both theoretical calculations[1,2,5] and experimental measurements.[3,4,6] All sources place the binding energy at above 150 meV for each of the three thicknesses. Additionally, our own calculations (described in the Computational Details section below) predict binding energies of ~190 meV for 3 ML CdSe NPLs, ~190 meV for 4 ML CdSe NPLs and ~170 meV for 5 ML CdSe NPLs, as shown in Table S2. The exciton binding energies from our calculations are in excellent agreement with the experimentally determined exciton binding energies reported in Refs. S3, S4, and S6.

The cyclotron energy is evaluated at 60 T, the highest magnetic field used in this work, using the relation

$$E = \frac{\hbar e B}{\mu_r} \tag{S1}$$

where $\hbar$ is the reduced Planck constant, e is the elementary charge, B is the magnetic field, and μ_r is the reduced mass of the exciton. Since the reduced mass of the exciton varies depending on the thickness of the NPL, the cyclotron energy varies for the different thicknesses. Reduced masses were calculated using the electron and heavy-hole masses reported in Ref. S2. Table 1 in the main text shows that the cyclotron energies are all roughly an order of magnitude less than the binding energies, indicating that 60 T is well within the low magnetic field regime for 3, 4, and 5 ML CdSe NPLs.

Table S1. Binding energies (BE) for CdSe NPLs reported in the experimental and theoretical literature.

Year of Publication	SI Ref. #	Experiment or Theory	3 ML BE (meV)	4 ML BE (meV)	5 ML BE (meV)
2012	S1	Theory*	200	175	158
2014	S2	Theory†	413	330	278
2015	S3	Experiment	-	178	-
2016	S4	Experiment	-	-	170
2017	S5	Theory	-	-	250
2019	S6	Experiment	230	210	130

* Using $\varepsilon_{out} = 2$, as is standard for organic ligands. As the outer dielectric constant increases, the binding energies drop, until they approach ~100 meV for all NPL thicknesses at $\varepsilon_{out} = 5$

† Using $\varepsilon_r^{\infty} = 6$

Table S2. Binding energies for 3, 4, and 5 ML CdSe NPLs of varying lateral sizes determined from atomistic electronic structure calculations.

ML	Lateral Dimensions (nm × nm)	Binding Energy (meV)
3	4 × 4	294
3	4 × 6	259
3	4 × 8	245
3	4 × 10	242
3	4 × 12	232
3	6 × 6	222
3	6 × 8	211
3	6 × 10	197
3	8 × 8	192
4	4 × 4	259
4	4 × 6	239
4	4 × 8	226
4	4 × 10	216
4	4 × 12	208
4	6 × 6	214
4	6 × 8	203
4	6 × 10	192
4	8 × 8	191
5	4 × 4	244
5	4 × 6	221
5	4 × 8	208
5	4 × 10	199
5	4 × 12	193
5	6 × 6	191
5	6 × 8	179
5	6 × 10	174
5	8 × 8	169

Absorption Spectra of Samples

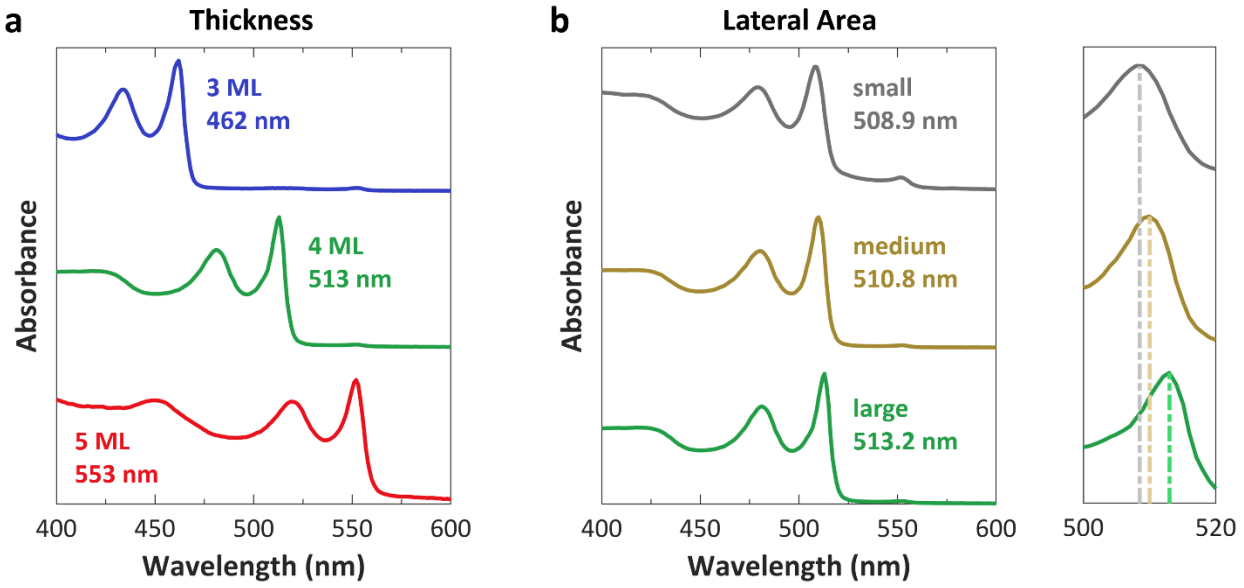

Figure S1. UV-vis absorption spectra at room temperature and no magnetic field of **(a)** 3, 4, and 5 ML NPLs and **(b)** small, medium, and large lateral-extent 4 ML NPLs. The right panel shows the slight shift in the heavy-hole exciton energy as the lateral size of the NPL increases.

SAXS Data for 3 and 4 ML NPLs

In the main text, SAXS data collected on polymer films containing 5 ML NPLs is presented. In addition to films containing 5 ML NPLs, films containing 3 and 4 ML NPLs were also analyzed using SAXS.

Figure S2 shows SAXS transmission and reflection data for 3 ML CdSe NPLs. Unlike the data presented in the main text for 5 ML CdSe NPLs, the SAXS data in Figure S2 does not present such a distinct ring near $q = 0.12$ Å^{-1}. It is possible that 3 ML NPLs do not stack as effectively as 4 or 5 ML NPLs; the larger lateral area of 3 ML NPLs has been shown to induce scrolling of NPLs, thereby prohibiting the stacking that would otherwise occur from van der Waals interactions of the flat areas. Nevertheless, stretching does seem to have an effect on alignment of 3 ML NPLs, as demonstrated by anisotropy in the reflection scattering along the vertical direction in Figure S2d.

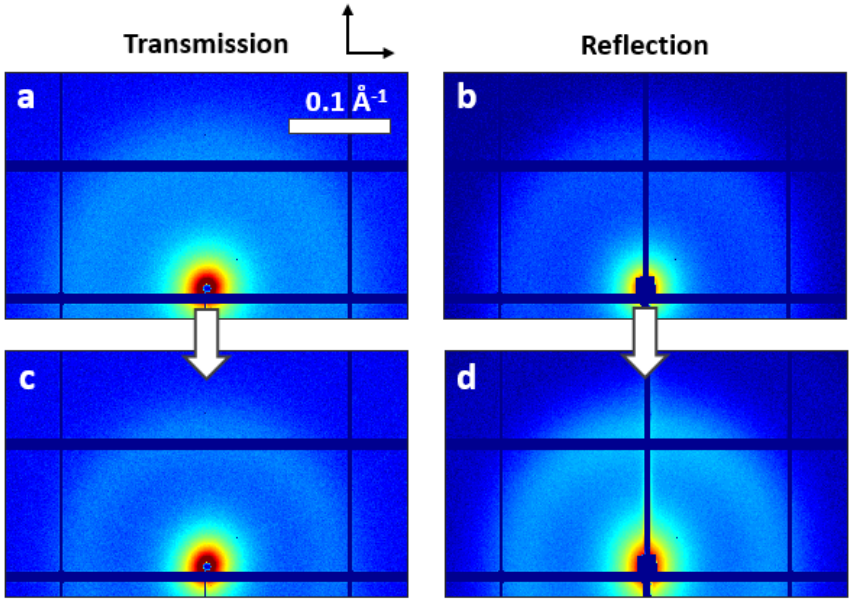

Figure S2. Transmission and reflection SAXS data for **(a, b)** unstretched and **(c, d)** stretched films containing 3 ML CdSe NPLs. Stretching axes are roughly indicated by the two black arrows. Intensities are logarithmic and not necessarily kept consistent between panels.

Figure S3 shows SAXS transmission and reflection data for 4 ML CdSe NPLs. Like the data presented in the main text for 5 ML CdSe NPLs, the SAXS data in Figure S3a,b initially indicate the presence of stacks of NPLs. The widening of the scattering peak in Figure S3c after stretching, and the weaker intensity at most azimuthal angles, suggests that many of the stacks are broken up after stretching. However, as in the main text, the reflection data in Figure S3d suggests that many NPLs have rotated from an alignment perpendicular to the plane of the film to one that is parallel.

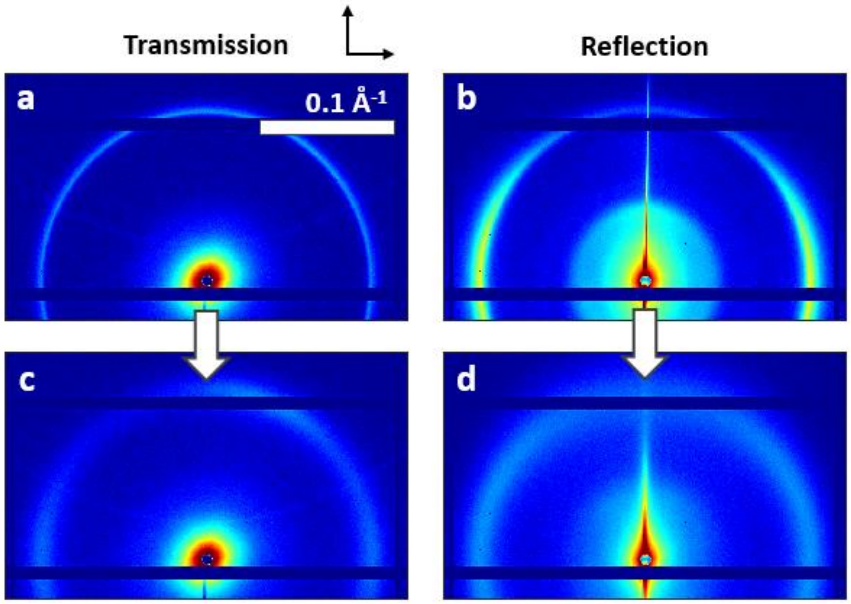

Figure S3. Transmission and reflection SAXS data for **(a, b)** unstretched and **(c, d)** stretched films containing 4 ML CdSe NPLs. Stretching axes are roughly indicated by the two black arrows. Intensities are logarithmic and consistent for each data collection mode before vs after stretching, but not between transmission and reflection modes.

Data Processing

Data were collected as transmission spectra as a function of wavelength. These spectra were then converted to energy space according to

$$E = \frac{hc}{\lambda} \tag{S2}$$

$$f(E) = -f(\lambda)\frac{hc}{E^2} \tag{S3}$$

where $f(\lambda)$ and $f(E)$ are the intensities at a given wavelength λ or energy E.[7] To describe the fitting procedure, the data set for 4 ML NPLs will be used as an example. Figure S4 highlights the entire fitting procedure for extracting out the peak shifts of the heavy-hole exciton peak.

Raw data for transmission spectra at 0 T, 26.2 T, and 58.9 T are shown in Figure S4a. For analysis, the data was truncated at some energy between the heavy-hole and light-hole peaks so that the only peak in the spectrum was that of the heavy-hole. The data was then normalized at an energy lower than that of the peak, as indicated in Figure S4b by the star. Two points on either side of the normalization point were selected as the two points needed to define the baseline, which is also shown in Figure S4b. The result of baseline subtraction is shown in Figure S4c; baseline subtraction helped fix the peak asymmetry brought upon by the fiber background, although the resulting peak was still slightly asymmetric. To counteract this, only the tip of the peak—which was mostly symmetrical—was fit, as shown in Figure S4d. Only the points below some count threshold (in the case of these 4 ML NPLs, -0.53 counts) were considered. The count threshold was selected by running the analysis at a range of count thresholds and then selecting the value that gave the smallest error for the diamagnetic shift. Each set of points was then fit to a Gaussian using the MATLAB (version R2016b) 'gauss1' fit function.

Using the peak positions obtained from the Gaussian fitting, the two sets of peak shifts (from the +60 T data and -60 T data) were fit to Eq. 1 in the text using nlinmultifit, a function provided through MATLAB File Exchange.[8] In this way, both sets of data were fit simultaneously to obtain E_0, g_{ex}, and σ. (Fitting g_{ex} and σ independently via $g_{\mathrm{ex}}\mu_B B = (E_+ - E_-)$ and $\sigma B^2 = \frac{1}{2}(E_+ + E_-)$ yields values that are within 2% of those obtained using nlinmultifit.) The inverse of the root mean square error (rmse) squared (i.e. the inverse variance) for each data point from the Gaussian fit was used as the weight in the fit. The 95% confidence intervals on σ are reported in the main text as the errors on the fit. These errors are believed to provide an accurate depiction of the error inherent to the measurement, as changing the count threshold returned a value of σ that was within the 95% confidence interval of the value reported in the text.

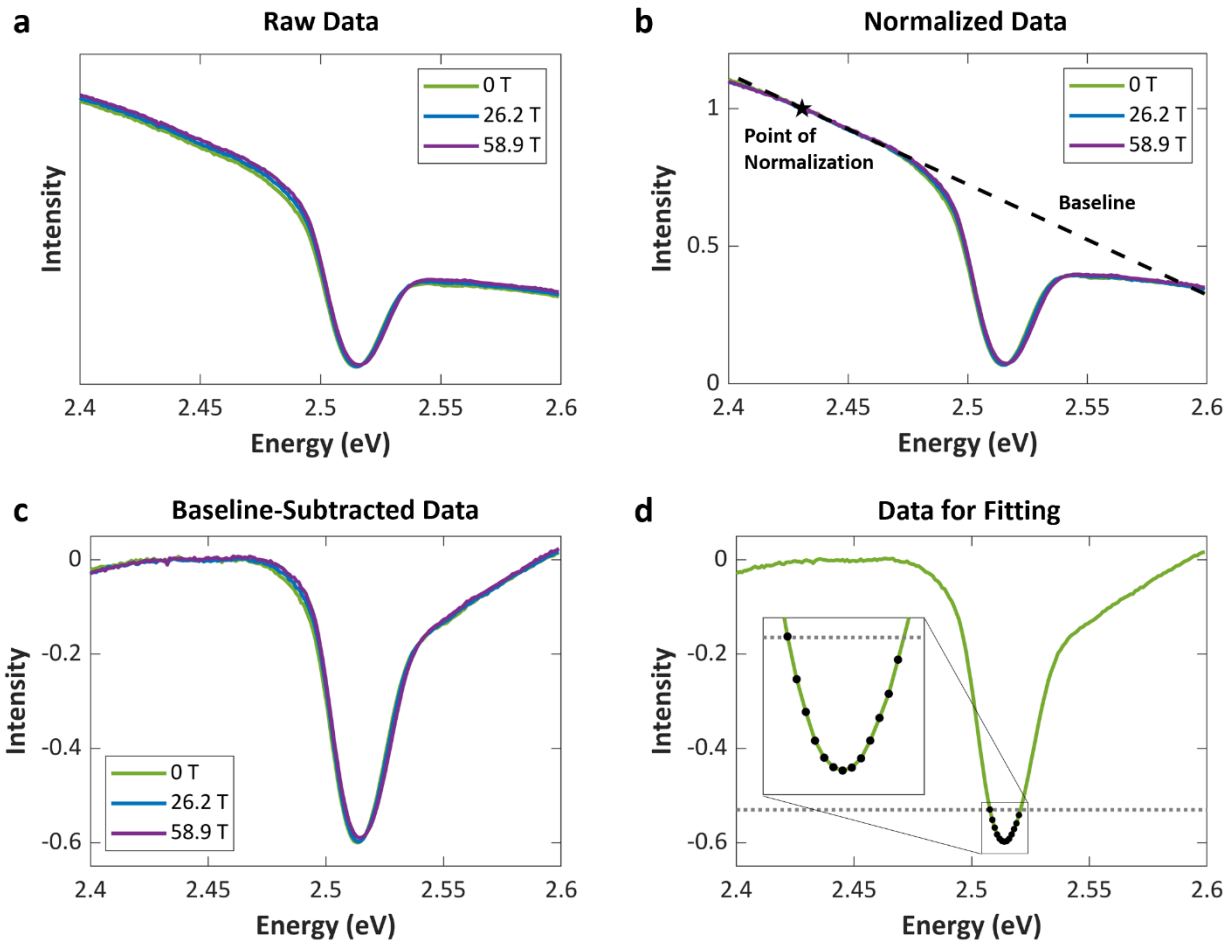

Figure S4. (a) Raw data. **(b)** Data normalized at the point marked by the star. The dashed line represents the baseline that was subtracted to yield the data in the next panel. **(c)** Baseline-subtracted data. **(d)** Baseline-subtracted data at 0 T, showing the points (black dots) below the count threshold (gray dotted line). Only the black points were fit to a Gaussian to determine the position of the peak.

Excitonic g-factors

Table S3 and Figure S5 present the excitonic g-factors obtained from fitting the magneto-optical data presented in the main text to Eq. 1. The g-factors display clear trends with thickness and lateral area, although their exact values varied when measuring different samples containing the same types of NPLs. This is likely due to the fact that the excitonic g-factor is anisotropic, with very little anisotropy present in the electronic g-factor but significant anisotropy present in the hole g-factor.[9,10] Given that different samples likely displayed varying degrees of orientation, it is expected that the variation in the alignment of the CdSe NPLs from one sample or another yield different excitonic g-factors. It is worth highlighting that despite the variation in magnitude, the trends presented in Table S3 were always preserved, such that it is likely that we were able to achieve a similar degree of orientation from one sample to another.

Table S3. Excitonic g-factors for 3, 4, and 5 ML and small, medium, and large 4 ML CdSe NPLs, obtained from fitting the data presented in the main text in Figure 4 to Eq. 1.

Thickness	Excitonic g-factor
3 ML	0.661 ±0.041
4 ML	0.320 ±0.013
5 ML	0.205 ±0.012

Lateral Area	Excitonic g-factor
small	0.185 ±0.030
medium	0.306 ±0.025
large	0.320 ±0.013

The trends presented in Table S3 can be rationalized in terms of known behaviors of excitonic g-factors with regards to size. As the thickness of the NPL decreases, the band gap increases, which results in a larger electronic g-factor but a constant hole g-factor.[9] As a result, the overall excitonic g-factor increases. The excitonic g-factor also increases with an increase in NPL area, where the increase in g-factor is particularly large for small vs medium NPLs, as opposed to medium vs large. This suggests that very small changes in lateral area have large effects on the electronic properties of the NPLs early on during their growth, while after a threshold size, the g-factors remain nearly constant in magnitude.

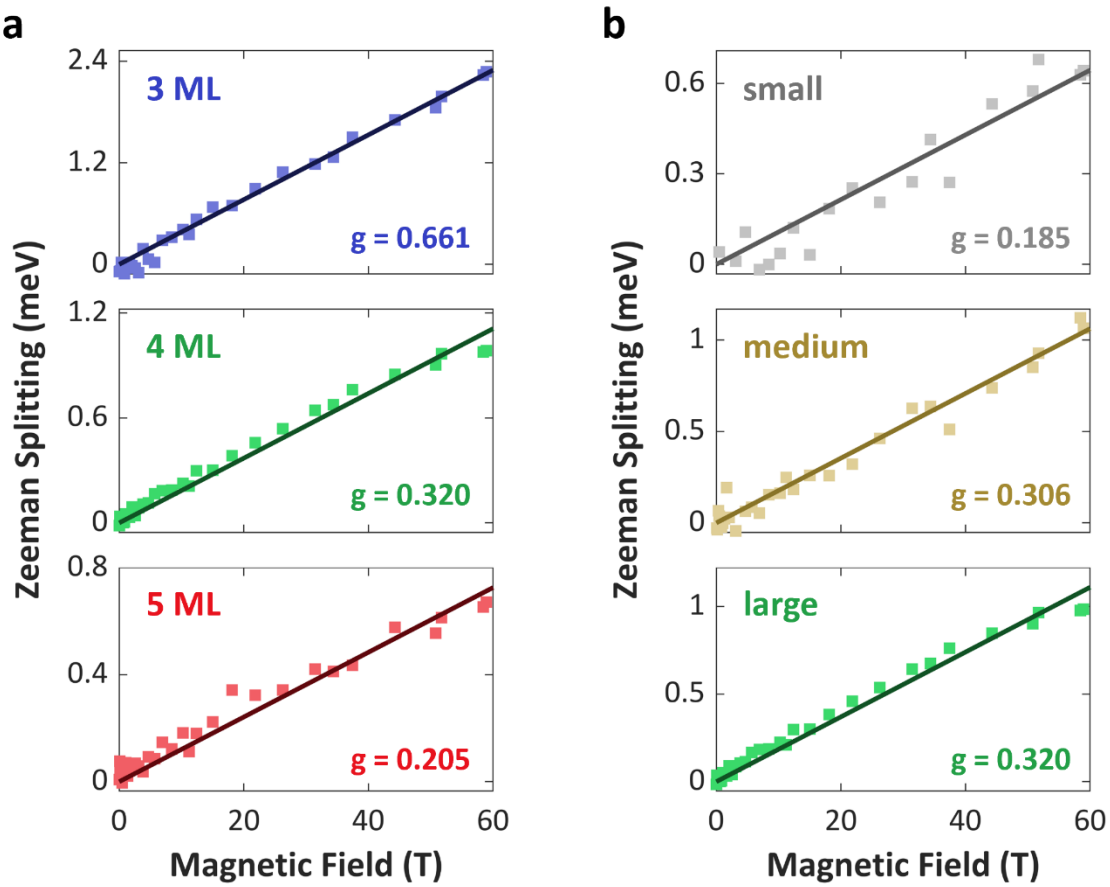

Figure S5. Zeeman splitting for all the samples, obtained by taking the difference between the excitonic energy as a function of field. The relation $g_{ex}\mu_B B = E_+ - E_-$ yields the reported excitonic g-factors. **(a)** Fits for the three different thicknesses: 3, 4, and 5 ML NPLs. **(b)** Fits for the three different lateral areas: small, medium, and large 4 ML NPLs.

Diamagnetic Shifts

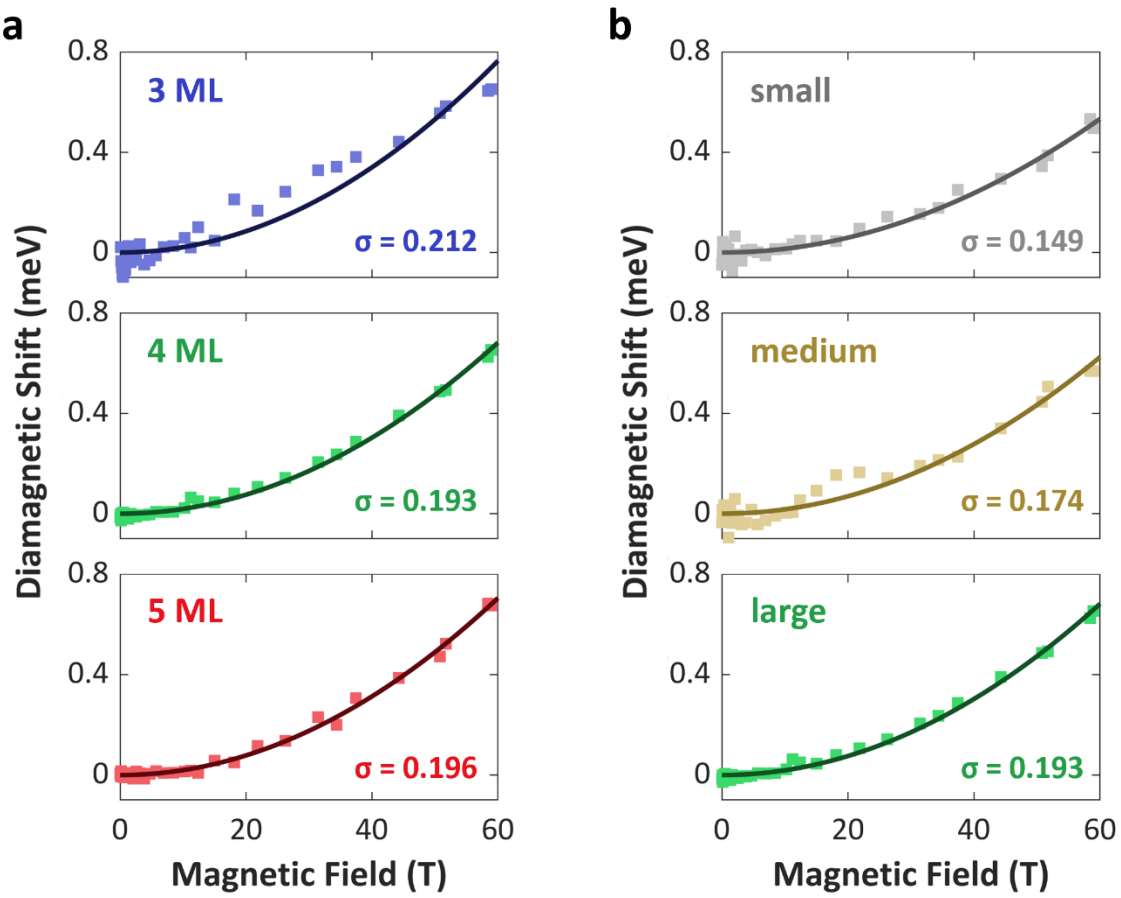

Figure S6. Diamagnetic shift, isolated by taking the average excitonic energy of the two states $E_{\text{avg}} = \frac{1}{2}(E_+ + E_-)$, for each sample. The shift can be fit to σB^2 to obtain a diamagnetic shift coefficient. **(a)** Fits for the three different thicknesses: 3, 4, and 5 ML NPLs. **(b)** Fits for the three different lateral areas: small, medium, and large 4 ML NPLs. Diamagnetic shift coefficients are indicated in units of μeV/T^2.

Computational Details

CdSe NPL configurations were created by cleaving a sufficiently large CdSe zinc blende crystal such that all Cd and Se atoms had at least two bonds and that both the top and bottom layers of the NPL were terminated with Cd. The surface of the NPL was then passivated using ligand potentials that were taken from Ref. 11. The ligands were placed in the correct geometry by using the positions of an extra outermost monolayer of Se and Cd atoms and replacing each Se (Cd) atom by the corresponding ligand potential for Cd (Se). The final NPL lengths, widths and thicknesses (and corresponding MLs) are given in Table S4.

We employed the semi-empirical pseudopotential method to obtain the noninteracting (i.e. single-particle) electron and hole states. These calculations were performed on real-space grids and converged with respect to the grid point density. Because we are only interested in the lowest energy excitonic states, we were able to use the filter-diagonalization technique[12,13] to calculate only the lowest energy electron (ϕ_a) and hole (ϕ_i) eigenstates. The eigenstates obtained from the application of the filter-diagonalization technique were then used as input to the Bethe-Salpeter equation (BSE).[13] The BSE was solved within the static dielectric constant approximation (ε = 5.00). Although the quantitative accuracy may improve if a more complicated approximation for the screening was used (e.g. the random phase approximation), we do not expect any qualitative changes. Specifically, it would be expected the dependence of r_{plane} with the number of MLs should hold, because if the screening were different between 3, 4 and 5 ML NPLs, it would be expected that the thinner NPLs would have the least amount of screening (i.e. lowest ε) which would lead to even smaller r_{plane} values for the thinner NPLs relative to the thicker NPLs. The output from solving the BSE are the excitonic states:

$$\psi(\vec{r_e}, \vec{r_h}) = \sum_{a,i} c_{a,i}\, \phi_a(\vec{r_e})\, \phi_i^*(\vec{r_h}) \tag{S4}$$

where ϕ_a (ϕ_i) are the single-particle electron (hole) eigenstates, $\vec{r_e}$ ($\vec{r_h}$) is the position of the electron (hole), and the coefficients ($c_{a,i}$) are obtained by solving the BSE. The number of electron (a) and hole (i) states needed to converge the calculations ranged from 50-350. More details on the BSE are given in Ref. S14.

After calculating the excitonic states (i.e. correlated electron-hole states), we then calculated the in-plane exciton size, $\langle r^2 \rangle$ as follows:

$$\langle r^2 \rangle = \langle \psi | r^2 | \psi \rangle \tag{S5}$$

$$\langle r^2 \rangle = \langle \psi | x^2 + y^2 | \psi \rangle \tag{S6}$$

$$\langle r^2 \rangle = \langle \psi | (x_e - x_h)^2 + (y_e - y_h)^2 | \psi \rangle \tag{S7}$$

Values for $\langle r^2 \rangle$ are reported in Table S4.

Table S4. Root mean square extents of the exciton in the x, y, and z directions, as well as the root mean square in-plane exciton radius r_{plane} for 3, 4, and 5 ML CdSe NPLs of varying lateral sizes.

ML	Lateral Dimensions (nm × nm)	$\sqrt{\langle z^2 \rangle}$ (nm)	$\sqrt{\langle x^2 \rangle}$ (nm)	$\sqrt{\langle y^2 \rangle}$ (nm)	$\sqrt{\langle x^2 + y^2 \rangle} = r_{\mathrm{plane}}$ (nm)
3	4 × 4	0.37	0.72	0.72	1.02
3	4 × 6	0.37	0.75	0.79	1.09
3	4 × 8	0.38	0.78	0.82	1.13
3	4 × 10	0.38	0.78	0.82	1.13
3	4 × 12	0.38	0.78	0.85	1.15
3	6 × 6	0.38	0.84	0.84	1.18
3	6 × 8	0.38	0.85	0.86	1.21
3	6 × 10	0.38	0.90	0.94	1.30
3	8 × 8	0.38	0.92	0.92	1.30
4	4 × 4	0.50	0.82	0.82	1.16
4	4 × 6	0.50	0.84	0.87	1.21
4	4 × 8	0.50	0.86	0.91	1.25
4	4 × 10	0.50	0.88	0.93	1.28
4	4 × 12	0.50	0.91	0.96	1.31
4	6 × 6	0.50	0.93	0.93	1.32
4	6 × 8	0.51	0.99	0.96	1.34
4	6 × 10	0.52	0.95	1.00	1.38
4	8 × 8	0.52	0.97	0.97	1.37
5	4 × 4	0.66	0.84	0.84	1.19
5	4 × 6	0.65	0.87	0.96	1.30
5	4 × 8	0.63	0.88	0.98	1.32
5	4 × 10	0.63	0.90	1.01	1.36
5	4 × 12	0.65	0.93	1.06	1.41
5	6 × 6	0.68	0.99	0.99	1.40
5	6 × 8	0.71	1.01	1.03	1.44
5	6 × 10	0.72	1.02	1.05	1.47
5	8 × 8	0.71	1.05	1.05	1.48

Effect of Dielectric Constant on Exciton Lateral Extent

The calculations described above use a value of $\boldsymbol{\varepsilon}$ = 5 as the high frequency dielectric constant. While the static dielectric constant of bulk CdSe is typically taken to be 10, the contribution from the nuclei ($\boldsymbol{\varepsilon}$ = 3.5) does not contribute as the energy scale of excitons is in the 100-200 meV range, which is much larger than the highest energy phonons for this composition. Furthermore, in quantum-confined materials, the dielectric screening is reduced, and our calculations have suggested that a dielectric constant of $\boldsymbol{\varepsilon}$ = 5 is most appropriate.

Nevertheless, as the value of the dielectric constant does impact the spatial extent of the exciton, we have performed additional calculations using ε = 10 to investigate the effect of altered dielectric screening. Table S5 compares values for the in-plane exciton radius for ε = 5 *versus* ε = 10. While the in-plane exciton radius is larger when the dielectric screening is increased to 10, the values (which range from 1.2 to 2.0 nm) are still significantly less than the bulk exciton Bohr radius of 5.4 nm for CdSe. Additionally, all of the qualitative trends for the in-plane exciton size are valid, irrespective of the choice of dielectric constant.

Table S5. Root mean square in-plane exciton radius r_{plane} for 3, 4, and 5 ML CdSe NPLs of varying lateral sizes, for different values of the dielectric constant.

ML	Lateral Dimensions (nm × nm)	r_{plane} (nm) for $\boldsymbol{\varepsilon = 5}$	r_{plane} (nm) for $\boldsymbol{\varepsilon = 10}$
3	4 × 4	1.02	1.22
3	4 × 6	1.09	1.39
3	4 × 8	1.13	1.43
3	4 × 10	1.13	1.45
3	4 × 12	1.15	1.50
3	6 × 6	1.18	1.61
3	6 × 8	1.21	1.69
3	6 × 10	1.30	1.74
3	8 × 8	1.30	1.79
4	4 × 4	1.16	1.36
4	4 × 6	1.21	1.47
4	4 × 8	1.25	1.53
4	4 × 10	1.28	1.60
4	4 × 12	1.31	1.62
4	6 × 6	1.32	1.60
4	6 × 8	1.34	1.69
4	6 × 10	1.38	1.79
4	8 × 8	1.37	1.79
5	4 × 4	1.19	1.34
5	4 × 6	1.30	1.53

5	4 × 8	1.32	1.60
5	4 × 10	1.36	1.63
5	4 × 12	1.41	1.69
5	6 × 6	1.40	1.76
5	6 × 8	1.44	1.85
5	6 × 10	1.47	1.89
5	8 × 8	1.48	1.96

References

(S1) Achtstein, A. W.; Schliwa, A.; Prudnikau, A.; Hardzei, M.; Artemyev, M. V; Thomsen, C.; Woggon, U. Electronic Structure and Exciton-Phonon Interaction in Two-Dimensional Colloidal CdSe Nanosheets. *Nano Lett.* **2012**, *12*, 3151–3157.

(S2) Benchamekh, R.; Gippius, N. A.; Even, J.; Nestoklon, M. O.; Jancu, J. M.; Ithurria, S.; Dubertret, B.; Efros, A. L.; Voisin, P. Tight-Binding Calculations of Image-Charge Effects in Colloidal Nanoscale Platelets of CdSe. *Phys. Rev. B* **2014**, *89*, 035307.

(S3) Naeem, A.; Masia, F.; Christodoulou, S.; Moreels, I.; Borri, P.; Langbein, W. Giant Exciton Oscillator Strength and Radiatively Limited Dephasing in Two-Dimensional Platelets. *Phys. Rev. B* **2015**, *91*, 121302(R).

(S4) Scott, R.; Achtstein, A. W.; Prudnikau, A. V.; Antanovich, A.; Siebbeles, L. D. A.; Artemyev, M.; Woggon, U. Time-Resolved Stark Spectroscopy in CdSe Nanoplatelets: Exciton Binding Energy, Polarizability, and Field-Dependent Radiative Rates. *Nano Lett.* **2016**, *16*, 6576–6583.

(S5) Rajadell, F.; Climente, J. I.; Planelles, J. Excitons in Core-Only, Core-Shell and Core-Crown CdSe Nanoplatelets: Interplay between In-Plane Electron-Hole Correlation, Spatial Confinement, and Dielectric Confinement. *Phys. Rev. B* **2017**, *96*, 035307.

(S6) Zelewski, S. J.; Nawrot, K. C.; Zak, A.; Gladysiewicz, M.; Nyk, M.; Kudrawiec, R. Exciton Binding Energy of Two-Dimensional Highly Luminescent Colloidal Nanostructures Determined from Combined Optical and Photoacoustic Spectroscopies. *J. Phys. Chem. Lett.* **2019**, *10*, 3459–3464.

(S7) Mooney, J.; Kambhampati, P. Get the Basics Right: Jacobian Conversion of Wavelength and Energy Scales for Quantitative Analysis of Emission Spectra. *J. Phys. Chem. Lett.* **2013**, *4*, 3316–3318.

(S8) Chen. Multiple Curve Fitting with Common Parameters using NLINFIT https://www.mathworks.com/matlabcentral/fileexchange/40613-multiple-curve-fitting-with-common-parameters-using-nlinfit?focused=6205126&tab=function (accessed Nov 18, 2017).

(S9) Tadjine, A.; Niquet, Y. M.; Delerue, C. Universal Behavior of Electron G-Factors in Semiconductor Nanostructures. *Phys. Rev. B* **2017**, *95*, 1–16.

(S10) Shornikova, E. V.; Biadala, L.; Yakovlev, D. R.; Feng, D. H.; Sapega, V. F.; Flipo, N.; Golovatenko, A. A.; Semina, M. A.; Rodina, A. V.; Mitioglu, A. A.; Ballottin, M. V.; Christianen, P. C. M.; Kusrayev, Y. G.; Nasilowski, M.; Dubertret, B.; Bayer, M. Electron and Hole G-Factors and Spin Dynamics of Negatively Charged Excitons in CdSe/CdS Colloidal Nanoplatelets with Thick Shells. *Nano Lett.* **2018**, *18*, 373–380.

(S11) Rabani, E.; Hetényi, B.; Berne, B. J.; Brus, L. E. Electronic Properties of CdSe Nanocrystals in the Absence and Presence of a Dielectric Medium. *J. Chem. Phys.* **1999**, *110*, 5355–5369.

(S12) Wall, M. R.; Neuhauser, D. Extraction, through Filter-Diagonalization, of General Quantum Eigenvalues or Classical Normal Mode Frequencies from a Small Number of Residues or a Short-Time Segment of a Signal. I. Theory and Application to a Quantum-Dynamics Model. *J. Chem. Phys.* **1995**, *102*, 8011–8022.

(S13) Toledo, S.; Rabani, E. Verly Large Electronic Structure Calculations Using an Out-of-Core Filter-Diagonalization Method. *J. Comput. Phys.* **2002**, *180*, 256–269.

(S14) Rohlfing, M.; Louie, S. G. Electron-Hole Excitations and Optical Spectra from First Principles. *Phys. Rev. B* **2000**, *62*, 4927–4944.